

Helium-plasma–Induced Straight Nanofiber Growth on HCP Metals

Shin Kajita

Institute of Materials and Systems for Sustainability, Nagoya University, Nagoya 464-8603, Japan

Tomohiro Nojima, Tatsuki Okuyama

Graduate School of Engineering, Nagoya University, Nagoya 464-8603, Japan

Yuta Yamamoto

Institute of Materials and Systems for Sustainability, Nagoya University, Nagoya 464-8603, Japan

Naoaki Yoshida

Research Institute for Applied Mechanics, Kyushu University, Kasuga, Fukuoka 816-8580, Japan

Noriyasu Ohno

Graduate School of Engineering, Nagoya University, Nagoya 464-8603, Japan

Abstract

Low-energy helium (He) plasma irradiations were conducted on ruthenium (Ru) and rhenium (Re), which have hexagonal close packed (HCP) crystal structures. Growth of linear shaped fiberform nanostructures were identified on the surfaces of the both metals after the He plasma irradiation. We also conducted He plasma irradiation while Re particles were deposited on tungsten substrate; 3-mm-thick large scale fiberform nanostructures were grown on the surface. The crystal orientation was analyzed using diffraction patterns of Re and Ru nanofibers together with detailed transmission electron microscope observations. It was found that the growth of linear nanofibers has a preferential crystal orientation in the growth direction and it is always in the *c*-direction of the HCP crystals. Potential growth processes and mechanisms are proposed based on the experimental observations.

1. Introduction

Helium (He) plasma irradiation leads to various morphology changes on metals caused by He bubble growth. The He irradiation effects were extensively investigated on tungsten (W), because it is the leading candidate material for plasma facing components in fusion devices, and the interaction with He ions is one of the important issues [1]. It was found that fiberform nanostructures (FNs) were grown when certain condition in terms of the surface temperature and the incident ion energy was satisfied [2, 3, 4]. The FNs can be formed on various metals such as molybdenum, iron, nickel, tantalum, rhenium (Re), rhodium, ruthenium (Ru), platinum, and so on [5, 6]. Helium-plasma–induced FNs are important not only in nuclear fusion research but also in various applications such as photocatalysis [7, 8, 9], photo absorber [10] and gas sensors [11]. However, the growth mechanism has yet to be fully understood.

Concerning the He induced FNs on W, it was often inferred that some diffusion process likely controlled the growth mechanism, because the thickness of the layer was proportional to the square root of the irradiation time [12, 13]. From experimental

observations, contributions of He bubble growth, surface diffusion, swelling by He absorption, and a digging process by rupturing of He bubbles have been discussed [14, 15]. Takamura *et al.* suggested the importance of bubble-made holes and loop-like structures [5]. From a modeling perspective, two conceptual models emerged that explain the phenomena for our understanding: visco-elastic model [16], which explained the fiber growth by viscous flow of W near the fiber surface, and adatom diffusion model [17, 18], in which the fiber growth was explained by the kinetics of adatom diffusion. The latter adatom effect has been supported with molecular dynamics (MD) simulations [19, 20], where it was shown that adatom island formations led to surface structuring. The visco-elastic model brought up the importance of the shear strength for the FN growth [21]. Experiments on various metals suggested that the FNs formation tend to occur easily on metals with high shear strength [5, 9].

Furthermore, the growth mechanism has been attempted to be explained by many large scale simulations, as was summarized well elsewhere [22, 4]. E.g., importance of ruptures/bursts of He bubbles for surface roughness was shown from MD and Monte Carlo simulations [23, 22]. Although initial growth can be explained well by simulations, growth to micrometer-thick

Email address: kajita.shin@nagoya-u.jp (Shin Kajita)

fiberform structures has yet to be fulfilled. In particular, because recent findings of large scale nanostructures called nanotendrils [24, 25, 26] and mm-thick fuzzy structures [27, 28], it became apparent that we have to revisit the growth mechanisms. In particular, it seems that pitting by He bubbles and swelling processes [15] or visco-elastic models cannot explain the growth of such large scale structures.

In this study, we have done He plasma irradiations to rhenium (Re) and ruthenium (Ru), which have hexagonal close-packed (HCP) crystal structures. On both surfaces, it has been pointed out that straight FNAs were formed by He plasma irradiation [5, 29, 30]. In this study, the temperature dependences of the morphology changes on Re and Ru are revealed, and, then, a growth of 3-mm-thick Re large-scale FNAs (LFNAs) with precipitation of Re during He plasma irradiation is shown. Based on transmission electron microscope (TEM) analysis, we will discuss the potential growth process of the straight FNAs during the He plasma irradiation.

2. Methods

2.1. He plasma irradiation

Experiments were conducted in the linear plasma device NAGDIS-II. Figure 1a shows a schematic of the experimental setup. It should be noted that the sputtering wire shown in Fig. 1a was used only for the precipitation experiments shown later and not installed in a conventional He plasma irradiation explained here. A 2-m-long cylindrical shaped He plasma was produced in a steady state, and samples were installed in the downstream of the linear device. The incident ion energy, E_i , which was determined by the potential difference between the sample and the plasma (space potential), was controlled by changing the biasing voltage. The surface temperature, T_s , which was measured with a radiation pyrometer, was controlled by changing the ion flux to the sample. Typically, when the surface temperature was less than 1000 K, a water-cooled sample stage was used to control the temperature. Concerning Re sample, 0.2 mm diameter wire (Nilaco Ltd.) was attached on a 0.2-mm-thick molybdenum sheet and exposed to the He plasma. We used 0.5-mm-thick Ru plate samples in this study.

2.2. Metal precipitation experiments

In addition to the conventional He plasma irradiation, formation of Re LFNA was demonstrated by installing a Re sputtering wire (0.2 mm in diameter) adjacent to a W sample, as shown in Fig. 1. The bias of the sputtering wire was -300 V so that the incident ion energy to the sputtering wire was sufficient to initiate sputtering of Re atoms. The energy was chosen to be lower than previous W LFNA cases [27] as considering the fact that the sputtering yield of Re is higher than that of W. We chose W for the substrate in this experiment, because Re substrate was not available and it was likely that growth of FNAs on the substrate was prerequisite for the LFNA growth [27].

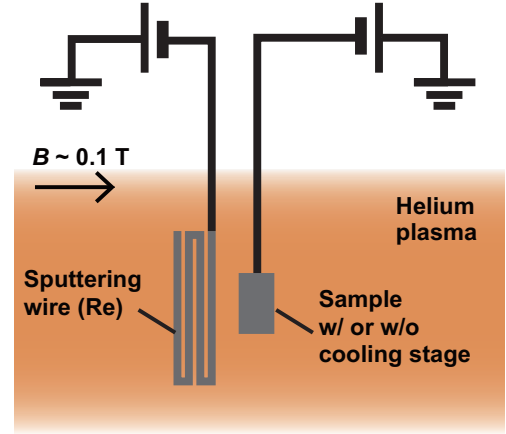


Figure 1: A schematic of the setup of He plasma irradiation.

2.3. Transmission electron microscope

Formed FNAs were observed by spherical aberration-corrected TEM/scanning TEM (STEM) (JEOL JEM-ARM 200F) [31] operated at an accelerating voltage of 200 kV. A focused ion beam (FIB) was not used to prepare TEM samples different from previous studies [14], because a coating is required before the FIB milling process. To observe the FNAs directly, a carbon micro-grid on a copper grid, which can be directly installed to TEM devices, was touched to sample surfaces to attach FNAs to the micro-grid. The sample holder was rotated in two directions, which crosses in 90° each other. When conducting diffraction pattern observation, the two angles were carefully aligned so that the electron beam vertically hits a crystal face of the fiber at a low Miller index. Selected area electron diffraction (SAED) patterns are used to analyze the crystal orientation of fibers. The projected size of aperture is ≈ 140 nm in diameter.

3. Nanostructure growth

3.1. Helium plasma irradiation

Figure 2a and b shows SEM micrographs of Ru and Re sample surfaces, respectively, that were exposed to He plasma. The irradiation conditions (E_i , T_s and the irradiation time, t_i) were as follows: a $E_i = 55$ eV, $T_s = 1000$ K, and $t_i = 7200$ s and b $E_i = 75$ eV, $T_s = 1220$ K, and $t_i = 1800$ s. FNAs were grown on the surface of the both samples. It seemed that the nanostructured layer was thin on the Ru sample as we could see the base of the substrate. On the other hand, FNAs fully covered the Re sample surface.

Figure 3a shows a temperature programmed desorption (TPD) spectrum of He from a Ru sample exposed to the He plasma. TPD spectra give us clues about He behaviors inside metals at different temperatures. The peak of the spectrum can be altered by changing the ramp rate. For example, in the case of W, peaks of He desorption at high (≈ 1000 K) and low (≈ 340 K) temperatures were shifted by ≈ 100 and 10 K, respectively, when the ramp rate was changed 0.1 to 2.0 K/s [32]. Here, we use desorption spectra as an indication of migration of He

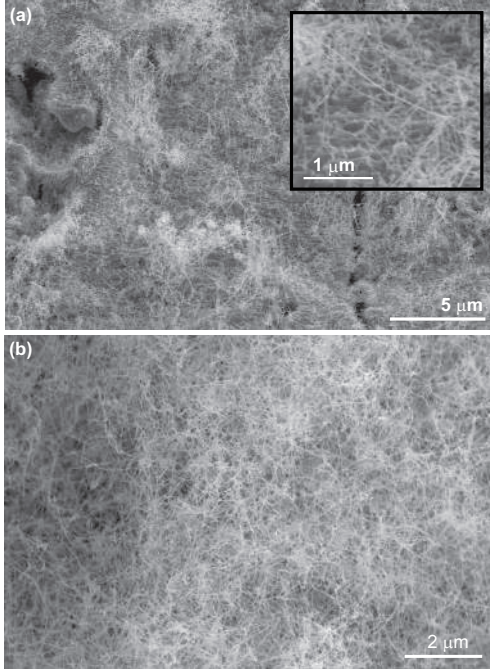


Figure 2: SEM micrographs of (a) Ru and (b) Re sample exposed to the He plasmas. The irradiation conditions are as follows: (a) $E_i = 55$ eV, $T_s = 1000$ K, and $t_i = 7200$ s and (b) $E_i = 75$ eV, $T_s = 1220$ K, and $t_i = 1800$ s.

atoms. Desorption started around 900 K, suggesting that migration of He atoms became active around that temperature. It had a peak at ≈ 1300 K and decreased gradually with increasing the temperature. When the temperature is too high, the migration of He atoms and surface diffusion are too active to form fine nanostructures for reference. Figure 4a-d shows SEM micrographs of Ru samples exposed to the He plasmas at different T_s indicated at red arrows in Fig. 3a. When T_s was 770 K (Fig. 4a), which was lower than the inset of He desorption, no significant surface morphology changes occurred. FNs were formed at 1000 K (Fig. 4b), and sub-micrometer sized roughness with finer structures were observed at 1130 K (Fig. 4c). The results indicated that temperature window of the formation of FNs for Ru was not so wide. Considering the fact that fine structures were identified, FNs may be formed around 1100 K, but it probably requires longer t_i or higher He ion flux. Previously, FNs were formed on 1- μm -thick Ru film with W substrate even when the temperature was 1190 K [30], which was higher than that of Fig. 4c. A fraction of W (roughly 10%) due to the diffusion of W to the Ru layer, could have increased the temperature range of the FNs growth. When T_s was 1490 K, which was higher than the peak temperature of ≈ 1300 K, the surface was still very rough and fiberform microstructures were identified on the surface.

Figure 3b shows a TPD spectrum of He from a Re sample exposed to the He plasma. Desorption started around 800–900 K and had a peak at ≈ 1200 K. The desorption spectrum was wider than that of Ru. Figure 5a-d shows SEM micrographs of Re samples exposed to the He plasma at different T_s . No significant morphology changes were caused by the He plasma irradiation when T_s was 690 K (Fig. 5a), FNs were identified at

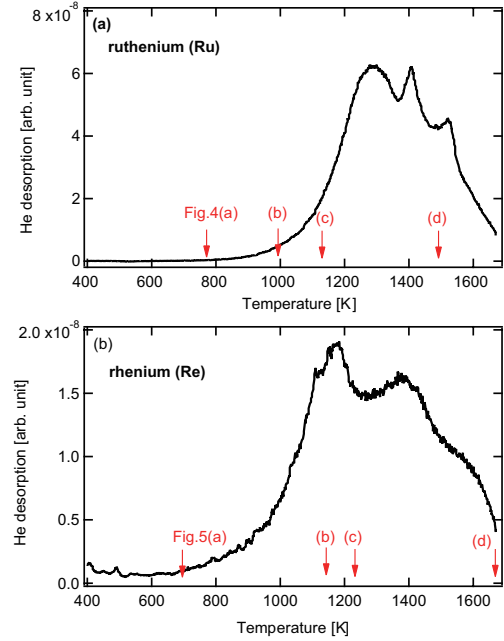


Figure 3: TPD spectra of (a) Ru and (b) Re sample exposed to He plasma at the heating rate of 1 K/s. The irradiation conditions are as follows: (a) $E_i = 85$ eV, $T_s = 1130$ K, and $t_i = 7200$ s, and (b) $E_i = 85$ eV, $T_s = 1130$ K, and $t_i = 7200$ s.

1130 and 1240 K (Fig. 5b,c), where desorption peaked, and fine structures were still observed at 1670 K (Fig. 5d). The width of the structure at 1670 K is greater than those at 1130 or 1220 K.

The wider desorption spectrum and morphology changes in this study revealed that the temperature window of Re for FN formation is wider than that of Ru. Previously, it was shown that 100 μm -thick FN layer was formed by 200 eV He ion irradiation to Re at 1040 K [29]. Thus, it is likely that Re is one of the easiest metals for the growth of FNs by He plasma irradiation.

3.2. Re precipitation experiments

Figure 6a shows a picture of the sample after an hour-long Re precipitation experiment. A 3-mm-thick LFN was grown on a W substrate after the exposure to He plasma and Re particles (neutrals and ions). The thickness of LFN was greater than that of W LFN cases, but the LFN did not expand so much to the surface direction compared with W LFN. Figure 6b and c shows SEM micrographs of the Re LFN at different magnifications. The LFN was mainly comprised of meshy structures. In contrast to W LFN, no membrane structure [33] was identified.

Figure 7a and b shows SEM micrographs of LFN in higher magnifications. Meshy structures were comprised of much finer FNs. Figure 7c shows an enlarged SEM micrographs in the yellow region in Fig. 7a. Fibers are longer than μm and curled. Bifurcation of fiber occurred less frequent than conventional W fuzz cases.

The LFNs are mechanically fragile and can be removed from the substrate easily, similar to conventional fuzz. Using another sample with Re LFNs that were formed under a similar condition, we estimated the mass density of Re LFNs. First, the mass of Re LFNs was measured from the mass change of

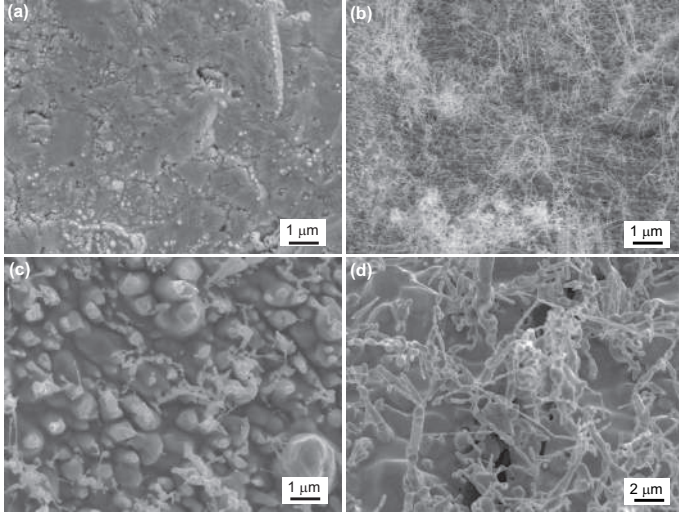


Figure 4: SEM micrographs of Ru samples exposed to the He plasmas. The irradiation conditions are as follows: (a) $E_i = 85$ eV, $T_s = 770$ K, and $t_i = 1800$, (b) $E_i = 55$ eV, $T_s = 1000$ K, and $t_i = 7200$ s, (c) $E_i = 85$ eV, $T_s = 1130$ K, and $t_i = 7200$, and (d) $E_i = 65$ eV, $T_s = 1490$ K, and $t_i = 3600$ s. (Note that the sample was tilted by 30° in (d).)

the sample by removing the LFNs. The volume was estimated using pictures of the sample taken from the top and side assuming that the averaged heights are half the peak heights viewed from a side of the sample. The mass of the LFNs was 1.01 mg, and the volume was 42.3 nm^3 ; the density was estimated to be 0.024 g/cm^3 , which was $\approx 0.1\%$ of the bulk density. Considering the fact that the density of W fuzz was 6% of the bulk when the thickness was $3 \mu\text{m}$ [34], the density of the LFNs was less than 1/10 of the conventional fuzz.

4. TEM observations

4.1. Nanofibers

First, we observed W nanostructures grown by He plasma irradiation to compare to Re and Ru FNs. Figure 8a and b shows a TEM micrograph and a high-angle annular dark field (HAADF)-STEM image of W nanofiber, respectively. Because HAADF-STEM is more sensitive to density variation [35], they are useful to observe inner structural changes. As can be clearly seen in Fig. 8b in particular, many He bubbles less than 10 nm in diameter existed inside the nanostructure. Because a nanometer-thick oxidized layer covered the surface, the surface border was not clear compared to other samples, as shown later. Lattice fringe can be seen on W nanostructures as shown in an inset in Fig. 8a, suggesting that the nanostructures has a crystal structure, as was discussed previously [7, 36].

Figure 8c and e shows TEM micrographs of nanofibers from Ru FN and Re FN samples, respectively. Hereafter, we call the nanofiber samples in Fig. 8c and e as Ru_{FN} and Re_{FN} samples, respectively. Figure 8d and f shows HAADF-STEM images of Ru_{FN} and Re_{FN} samples, respectively. Ru_{FN} sample surface was smooth with a roughness of one or two atomic scale, while Re_{FN} sample surface was rougher with a roughness of several nm. Nano-bubbles can be scarcely identified on Ru_{FN}

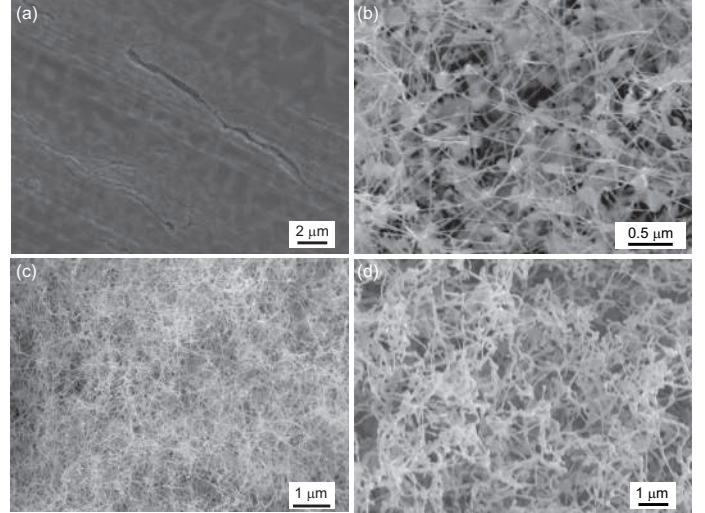


Figure 5: SEM micrographs of Re samples exposed to the He plasmas. The irradiation conditions are as follows: (a) $E_i = 55$ eV, $T_s = 690$ K, and $t_i = 660$ s, (b) $E_i = 55$ eV, $T_s = 1130$ K, and $t_i = 2200$ s, (c) $E_i = 75$ eV, $T_s = 1220$ K, and $t_i = 1800$ s, and (d) $E_i = 75$ eV, $T_s = 1670$ K, and $t_i = 1800$ s.

and Re_{FN} samples. On Ru_{FN} sample, elongate bubbles in transverse direction of the fiber were found. Similar elongate bubbles were found on Rh FN previously [6], indicating that this phenomenon was not peculiar to Ru or HCP metals. However, such elongation of bubbles has never been clearly identified from experiments on W cases, though hexagonal He bubbles were found on W substrate when the surface temperature was rather high [14]. Note that it has been shown in MD simulations that bubbles on W tend to elongate toward the surface, typically along $\langle 111 \rangle$ direction [19, 20]. It is likely that bubbles can be grown easier in transverse direction than the axial direction in Ru or some other metal cases. No such elongate bubbles were found on Re_{FN} sample.

The surface energy anisotropy, which was discussed recently as related to He-plasma induced morphology changes by Parish *et al.* [37], may be related to the elongation of bubbles. Although different references reported different values, it was likely less than 35% on major planes. The anisotropy has been calculated on various HCP metals including Ru and Re [38, 39]. It was reported that the basal plane (0001) for Re and the secondary prism plane for Ru have the minimum surface energy. Especially, for Ru case, the secondary prism plane has less than half the surface energy of the basal plane. However, because the elongation direction of He bubbles would corresponds to the basal plane direction considering the crystal orientation analysis shown later, the direction seems unreasonable if the secondary prism plane has the minimum value. Although it is difficult to explain the elongation from the view point of surface energy, further discussion considering the temperature dependence of the free energy and the critical resolved shear stress in the slip planes is of interest.

Figure 9a and b shows TEM micrograph and HAADF-STEM image of Re nanofiber, respectively, that were formed by Re precipitation experiments shown in Figs. 6 and 7. The sample is called Re_{LFN} sample hereafter in this paper. Lattice fringe can

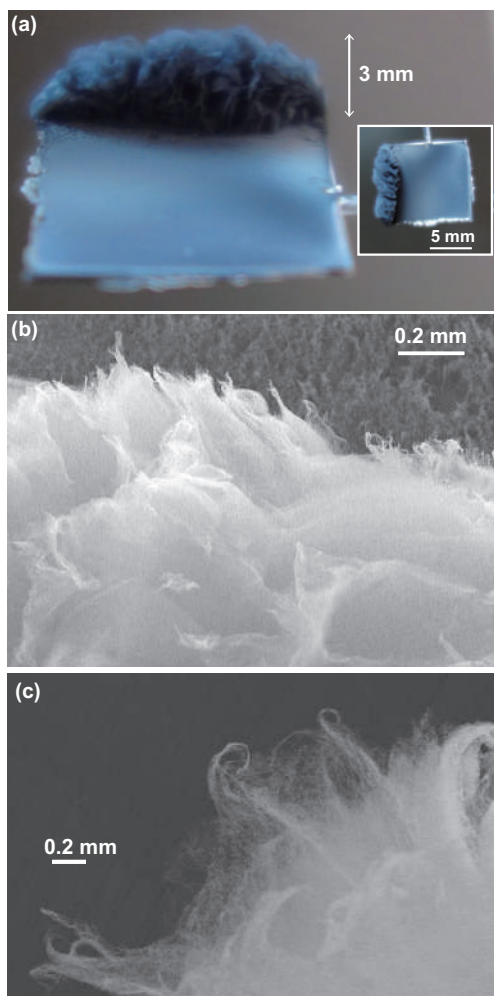


Figure 6: (a) A picture of the W substrate with Re LFN, and (b,c) SEM micrographs of the Re LFN.

also be clearly identified on Re_{LFN} sample, suggesting that the FN has a crystal structure. Different from Re_{FN} sample, many bubbles existed inside the fiber. Not only elongate bubbles in transverse direction of the fiber, but also round shaped bubbles existed inside the fiber. The roughness of typically 1 nm existed on the fiber surface; it was much smoother than that of Re_{FN} sample shown in Fig. 8e.

The surface roughness could be dependent on the material temperature during the irradiation, because the surface diffusion is altered by the temperature. E.g., the rough surface identified on Re_{FN} (Fig. 8e) may become smoother similar to the one shown in Fig. 8a when increasing the temperature further. In this study, we will focus on the crystal orientation of nanofibers of Ru_{FN} , Re_{FN} , and Re_{LFN} samples.

4.2. Amorphous clusters

When observing Re_{FN} and Re_{LFN} samples carefully by TEM, we identified many dusts, which had different features than nanofibers, clung on the surface of fibers. In this study, we call these as clusters. Figure 10a shows a TEM micrograph of Re_{FN} sam-³⁰⁰ple. A flat cluster with the size of 100 – 200 nm is seen in the

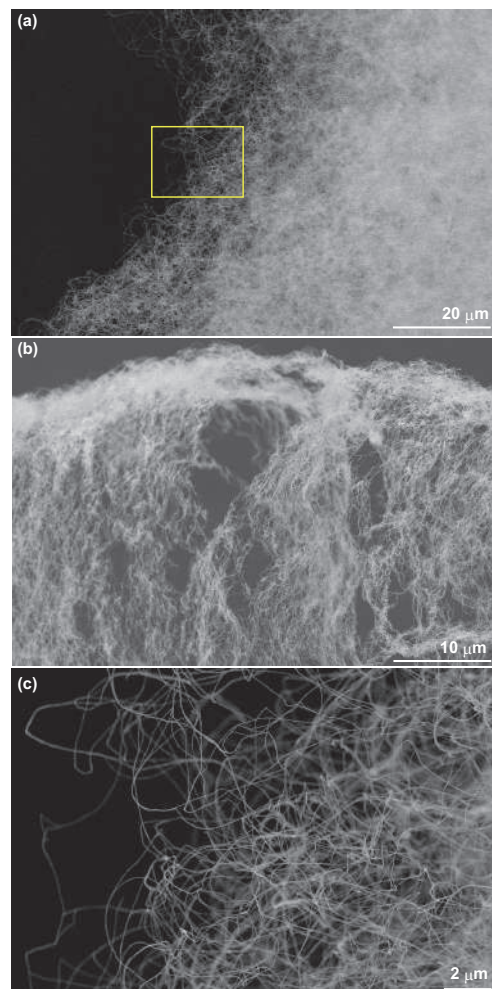


Figure 7: SEM micrographs of LFN formed by Re precipitation experiments.

intersection of fibers. It is likely that the thickness of the cluster is similar to the fibers (10 – 20 nm) from the brightness of the image. An inset shows the diffraction pattern of the cluster. Only ring shaped diffraction pattern was seen, suggesting that the cluster was amorphous. Figure 10b shows a TEM micrograph of Re_{LFN} sample; clusters were identified on Re_{LFN} sample as well. Figure 10c shows a TEM micrograph of the cluster clung on Re_{LFN} fiber, and the inset shows its diffraction pattern. The diffraction pattern shows a ring structure in addition to some pattern, suggesting that the cluster was not entirely amorphous but not entirely crystalline either. Hereafter, we call it an amorphous-like structure in this study.

We conducted energy-dispersive X-ray spectroscopy (EDS) analysis of the amorphous-like and pure fiber parts. On both clusters attached on Re_{FN} and Re_{LFN} samples, the atomic fraction of oxygen was higher than the fiber part and was $\approx 67\%$. During the discharges in the NAGDIS-II devices, the fraction of oxygen was very low, on the order of 100 ppm [40], and the temperature of the sample should be higher than the melting points of rhenium oxides during the irradiation. Therefore, it is unlikely that oxides were formed while the sample was exposed to the He plasma; the amorphous-like structure would rather be

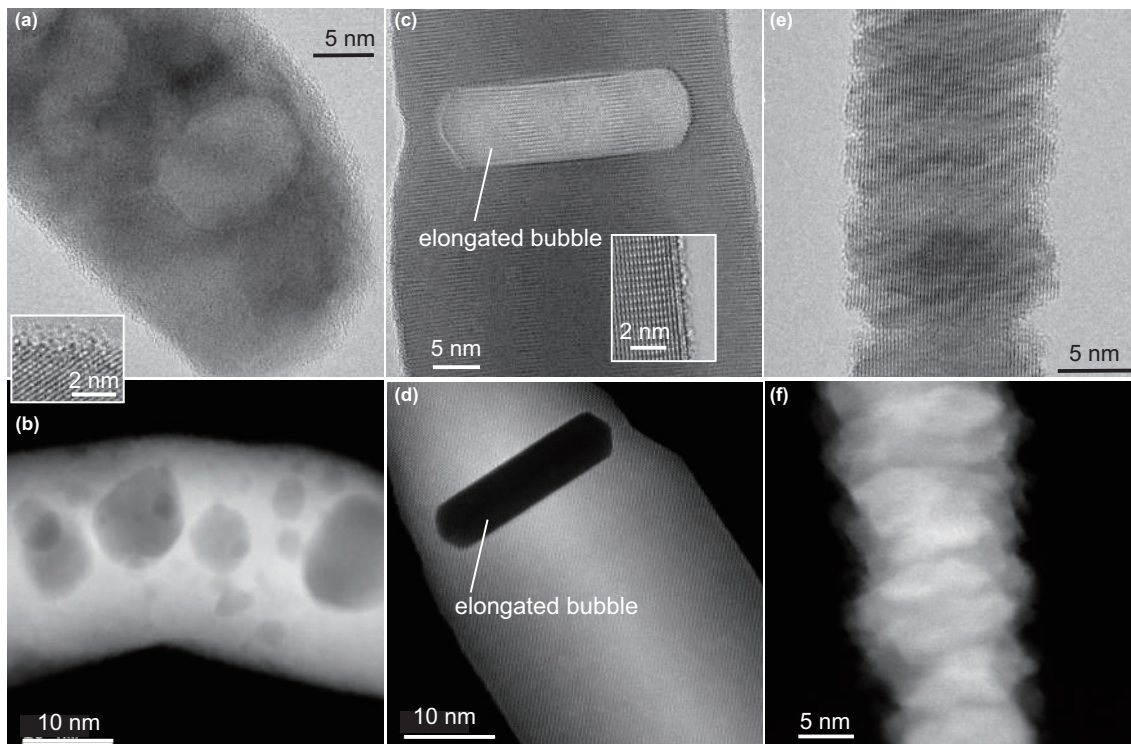


Figure 8: (a-c) TEM micrographs (d-f) and high-angle annular dark field (HAADF) -STEM image of nanofibers from W FN, Ru FN, and Re FN, respectively.

oxidized after the irradiation. In other words, they could be oxidized much more easily in the atmosphere than fiber part, which has a definite crystal structure. Only Re was identified on Re_{LFN} sample, and small amount ($< 2\%$) of Mo was found on a Re_{FN} sample. However, no difference was identified in the metallic contents between the fiber and cluster parts on both of Re_{FN} and Re_{LFN} samples.

These amorphous-like structures are quite different from the nanofibers, which have always a clear crystal structure. It is at the moment unclear whether those amorphous-like structures have contributed to the growth of FNs/LFNs. They could be just formed while adatoms diffused on the surface especially in intersection area of nanofibers. However, because the size would be too large for cluster diffusion [41], it was unlikely that the cluster moved during the irradiation, while the shape could be altered. Because the sizes were almost the same, typically 100 nm, some mechanism might have existed to determine the size (growth and shrinking).

4.3. Crystal orientation

Figure 11a-c is SAED patterns of Ru_{FN} , Re_{FN} , and Re_{LFN} samples, respectively. The patterns were taken from the parts marked with red circles in insets. The central brightest spot in diffraction patterns correspond to the transmission wave. Diffraction spot can be formed from the crystal surfaces which satisfy Bragg condition. Since the distance between the diffraction spots in reciprocal space corresponds to the distance between crystal faces, face indexing can be done using the diffraction pattern. We used a crystallography free software ReciPro [42] for face indexing.

From Fig. 11a, the distances between two spots in the two axes directions, i.e L_1 in the fiber axis direction and L_2 in the perpendicular direction to the fiber axis, were deduced to be 9.2 and 8.3 nm^{-1} , respectively. It was found that the growth direction corresponded to the $\langle 0001 \rangle$ direction, which is c -direction in HCP crystal structure. We performed face indexing at two more different locations; the result was consistent with that in Fig. 11a. Similarly, the face indexing was performed on a Re nanofiber shown in the inset of Fig. 11b. From the fact that $L_1 = 9.0 \text{ nm}^{-1}$ and $L_2 = 14.8 \text{ nm}^{-1}$, it was found that the growth direction was also in the c -direction on Re nanofibers. The same analysis was performed on nine other locations, and the growth direction was always in the c -direction. Figure 11c shows an SAED pattern of Re_{LFN} sample shown in the inset. From the SAED pattern, $L_1 = 8.9 \text{ nm}^{-1}$ and $L_2 = 8.1 \text{ nm}^{-1}$, suggesting that the growth direction was also in the c -direction. The same analysis was conducted for ten other locations for Re_{LFN} sample, and the c -direction growth occurred on all the locations.

Diffraction pattern of Re_{LFN} sample had slightly different from that of Ru_{FN} or Re_{FN} . Splits occurred on diffraction spots, probably because the direction of fibers changed slightly in a scale smaller than the aperture size of 140 nm. Because the two split spots were not far from each other, the variation in the direction was not so large, say 5° . Because the growth rate of LFN was greater than that of conventional FNs by 2-5 orders of magnitude [27], variation in the growth direction occurred more frequently compared with the conventional FN growth. The results of the growth direction analysis are summarized in table 1. The experiments revealed that the growth direction has

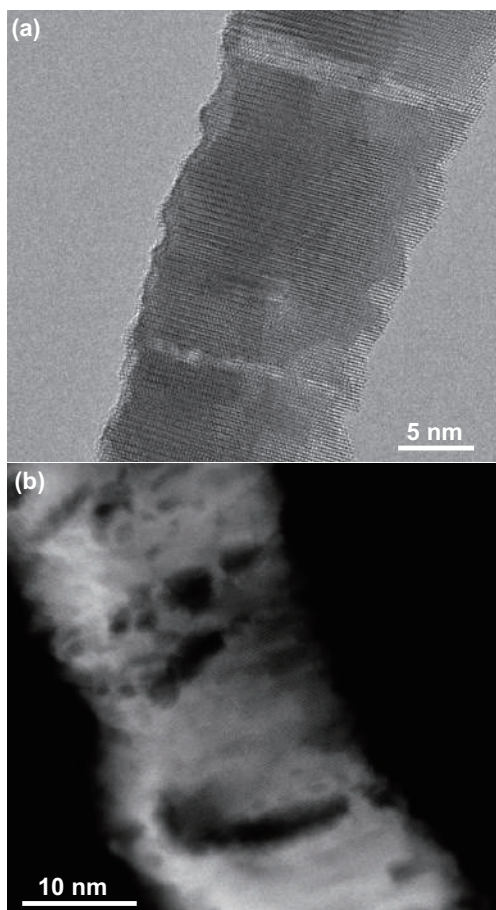


Figure 9: (a) TEM micrograph and (b) HAADF-STEM image of Re LFN formed by precipitation experiment.

Table 1: Summary of the growth direction analysis.

Sample	Number of analyzed fibers	Preferential growth orientation
Ru _{FN}	3	<i>c</i> -axis
Re _{FN}	10	<i>c</i> -axis
Ru _{FN}	11	<i>c</i> -axis

a preferential crystal orientation in *c*-direction on the straight FNs found on Ru and Re samples.

4.4. Discussion

What is the mechanism for the growth of Re and Ru FNs by He plasma irradiation or FNs growth by He plasma irradiation in general? Here, based on the experimental results, we try to discuss the possible mechanisms.

Before discussing FN growth by He plasma irradiation, three different mechanisms for nano-sized fiber/whisker structural growth are briefly referred here for comparisons: carbon nanotubes (CNTs), tin (Sn) whisker, and molecular beam epitaxy (MBE). Figure 12a-c presents schematics depicting the growth mechanisms of CNT, Sn whiskers, and MBE, respectively, from references [43, 44, 45]. CNTs by chemical vapor deposition (CVD)

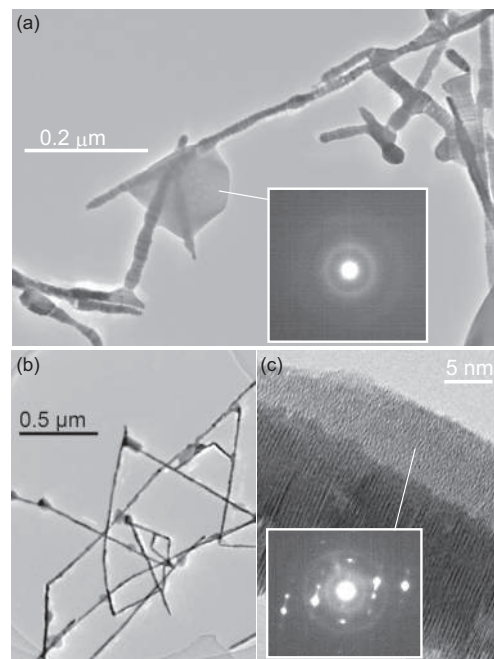


Figure 10: TEM micrographs of (a) Re_{FN} sample and (b,c) Re_{LNF} sample. Amorphous like clusters were adhered on the nanofibers.

has a similar feature and has been well investigated [43]. Although the growth condition is quite different from that of metallic FNs and the chemistry of carbon is different from that of metals, it is worth taking a look at it to introduce the various possibilities to discuss the potential mechanism. In the most widely-accepted CNT growth model, it was assumed that metal nano-particles adsorbed hydrocarbon vapor. A supersaturation of carbon species in the liquid metal nano-particle plays a catalytic role and precipitate to form carbon cylinder. For the CNT formations using catalyst nano-particles, both of bottom-growth and tip-growth are possible depending on the catalyst-substrate interaction. As one of similar fiberform growth, Sn whisker growth have also been investigated [46, 44]. It is well accepted that internal stresses in low-melting-point metals promote whisker growth through a creep-like process [46, 47], as shown in Fig. 12b. In addition, for metal whiskers, the energy gain due to the electrostatic polarization of metal filaments in an electric field was suggested to be worked [48]. In either way, the process is bottom-growth process; atoms are always supplied from the substrate from the bottom of nanofibers. Concerning MBE, which make it possible the growth of semiconductor nanowires including Si and GaAs [49, 45], it is regarded that diffusion of adsorbed atoms (adatoms) contributes to the growth of nanofibers on the tip (tip-growth) (Fig. 12c).

For conventional He induced FNs, the growth of protrusions occurs in the initial phase due to He bubble growth and bursting as well as swelling processes [50, 51, 15]. This process is likely similar to the Sn whisker growth process; the stress inside metal by He bubbles pushes up fiberform structures such as shown in Fig. 12b. Or, the visco-elastic model [16], in which newly created bubbles create an excessive force to form a flow in skin of fibers, may be applied to the initial growth process. How-

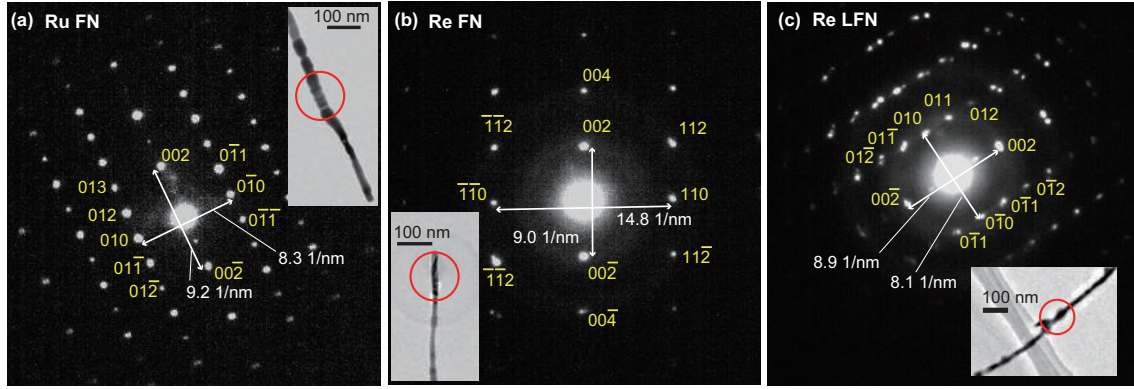


Figure 11: Diffraction patterns of (a) Ru FN, (b) Re FN, and (c) Re LFN samples. The patterns were taken from red marked regions in insets.

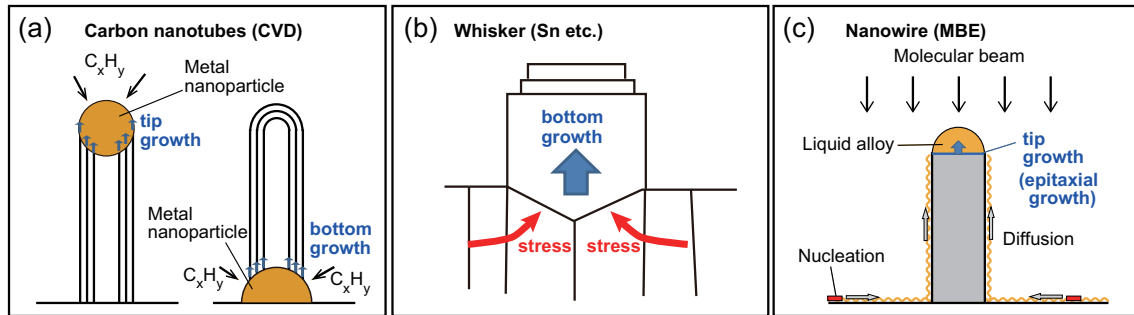


Figure 12: Schematics representing the well-accepted growth processes of (a) carbon nanotubes by chemical vapor deposition process [43], (b) Sn whisker [46], and (c) a nanowire by molecular beam epitaxy [45]. These are redrawn based on schematics in above references.

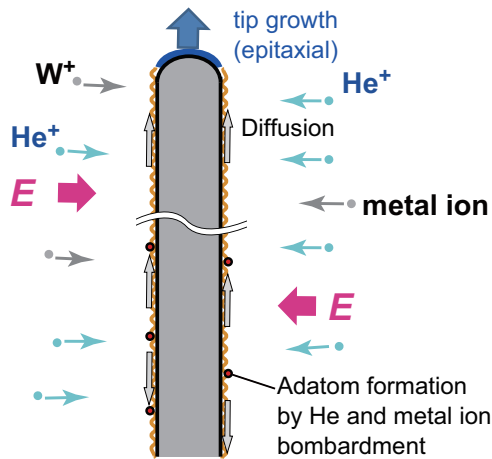


Figure 13: A schematic of the proposed growth process of He induced LFN.

ever, because almost no bubbles were found inside Ru_{FN} and Re_{FN} samples and the enhanced growth occurred by precipitation of Re particles, other mechanism should have worked for the growth to thicker Re and Ru FN layer and LFNs.

In the case of MBE, adatoms are produced on the substrate base by molecules from a molecular beam. For pure He plasma irradiation, adatoms can be formed by He ion bombardment [52]. Most of the adatoms were likely formed on the base of the sample, because recent experiments using tracer gas (3He) [53] suggested that He ions could be penetrated to the base

even when FNs layer was 3- μm -thick. For LFNs, on the other hand, adatoms can be formed by deposition of metallic ions in addition to the bombardment of He ions. Different from conventional FNs, experiments suggested that the adatoms can be formed on fiber surfaces. It was observed that the growth rate exponentially increased with t_i in the initial phase of the growth of W LFNs until the height of the structure became comparable to the sheath thickness [28]. This is most likely because an electric field formed around the nanofiber starts to attract ions when the structure size is greater than the sheath thickness, and, subsequently, metal ions precipitate on the fiber surfaces directly together with He ions [27]. The precipitated metal ions form adatoms on the fiber surface and start to diffuse on the fiber surface. Thus, diffusion of adatoms is not required for fiber growth, and the number of adatoms on the fiber surface can be much greater than those formed in pure He plasma irradiation cases. This would result in the increase in the growth rate by 2–5 orders of magnitude from that in the conventional FNs [27].

One thing that we would like to check here is that the experimental observations of LFNs support a tip-growth model. It is difficult to explain the exponential increase in the growth rate of LFNs with the bottom-growth models such as the ones shown in Fig. 12c or the right model in Fig. 12a in the current understanding. If the adatoms formed on the fiber surface could contribute to the growth only in a bottom-growth manner, the growth rate of LFNs should decrease with t . The tip-growth model is plausible for the conventional FNs as well. Similar to the MBE case (Fig. 12c), formed adatoms on the base can con-

tribute to growth after the diffusion on the fiber surface. The fact that the thickness of the FN layer increased proportional to $t_i^{1/2}$ could reflect this diffusion process of adatoms along fibers [12], as was presented by Trufanov using an MD simulation [18].

Finally, the present study found that Ru FNs and Re FNs/LFNs always have crystal structures and they have preferential crystal orientation in the growth axis. The results suggested that growth occurs in the axial direction of fibers, preserving the crystal structure of the fiber tip. In other words, it is highly likely that epitaxial crystal growth occurs on the fiber tips when adatoms reach them, similar to MBE cases. Figure 13 is a schematic representing the proposed growth process of He-induced LFN. When the structure size is comparable to the sheath thickness, an electric sheath starts to form around the fiber. Metal and He ions are collected by the electric field and adatoms form on the fiber surfaces. The adatoms diffuse on the fiber surfaces and contribute to the growth via epitaxial crystal growth when they reached the fiber tip.

Although epitaxial growth is the best idea to our knowledge, we should assume some special condition for the tip of fibers to be the trap site of adatoms. In the CVD or MBE cases, it is assumed that liquid nanoparticles play an essential role to drive the growth of nanofibers on the tip. However, the present situation is different from those cases. Martynenko *et al.* discussed that tip of nanofibers and thin shells of unopened bubbles can be trap sites for adatoms in terms of chemical potential [17]. Further investigation including detailed TEM observations of tip of fibers are required to reveal the mechanism of the entire growth process.

One of major differences between whisker/CNT and He induced FN/LFN in their features is in the fact that bifurcations, kinks, and bending of nanofibers occur frequently on FN/LFN. We thought that kinks and bending were caused by the influence of pressurized He bubbles inside the nanofibers. Concerning bifurcations, an observation of Ru FN in previous study showed that many He bubbles were frequently observed on node parts of nanofibers [6]. Thus, it is also likely that He bubbles contributed to the bifurcations. Distortion of crystal structure by He bubbles might form another growth face in different direction from the original fiber axis. Furthermore, on non-HCP metals, considering the fact that no preferential growth direction was found in the cases of W [36, 54], which has a body-centered cubic (BCC) lattice, bifurcations can occur any locations.

5. Conclusions

In this study, we performed He plasma irradiation to form FNs on Ru and Re surfaces. Moreover, by precipitating Re particles (ions and neutrals) together with He ions on W substrates, we showed that a 3-mm-thick Re LFN layer was formed. Primarily, linear shaped 10 – 20 nm width nanofibers comprised the FNs/LFNs. The TPD spectra from Ru and Re samples that were exposed to He plasmas showed that the temperature range of desorption from Re sample was wider than that of Ru sample, and the temperature range to cause FN growth was wider on Re (1130 – 1670 K) than that on Ru, on which FN growth was

identified at ≈ 1000 K; the results suggest that the temperature window of Re for FN formation is wider than that of Ru. From TEM observation of FNs, it was found that almost no bubbles existed inside the linear shaped Ru and Re nanofibers, while many nano-sized bubbles were identified in Re LFNs. We determined the crystal orientation of FNs/LFNs from the diffraction pattern. It was found that the fiber axis of FNs/LFNs was always in *c*-direction. Different from W case [36], where no preferential crystal orientation in the growth direction was found, Re and Ru, which has HCP crystal structure, have a clear preferential growth orientation. Based on the experimental observations, we discussed the potential growth mechanism as comparing with growth mechanisms of several typical nanostructures (Sn whisker, CNTs growth by CVD, and nanowhiskers by MBE). The nanofibers always have crystal structure with preferential growth orientation; it is suggested that the epitaxial growth is the growth mechanism of nanofiber. Adatoms can be formed on the side surface of nanofibers on LFN cases by the bombardment of He ions and metallic ions, and diffused adatoms can result in the growth on the tip of the nanofibers. Assuming that the conventional FNs are the same growth mechanism as the LFNs, it is likely that adatoms formed on the bulk surface diffused to and contribute to the crystal growth on the tip of fibers for conventional He induced FNs.

Acknowledgement

The authors thank Dr. Kuwabara for supporting TPD experiments and Dr. Tanaka for useful discussion. This work was supported in part by a Grant-in-Aid for Scientific Research 15H04229, Grant-in-Aid for Exploratory Research 16K13917, Fund for the Promotion of Joint International Research 17KK0132 from the Japan Society for the Promotion of Science (JSPS), and JSPS Bilateral Joint Research Project.

References

- [1] Y. Ueda, J. Coenen, G. D. Temmerman, R. Doerner, J. Linke, V. Philipps, E. Tsitron, Research status and issues of tungsten plasma facing materials for iter and beyond, *Fusion Engineering and Design* 89 (7) (2014) 901 – 906. doi:<https://doi.org/10.1016/j.fusengdes.2014.02.078>. URL <http://www.sciencedirect.com/science/article/pii/S0920379614001859>
- [2] S. Takamura, N. Ohno, D. Nishijima, S. Kajita, Formation of nanostructured tungsten with arborescent shape due to helium plasma irradiation, *Plasma and Fusion Research* 1 (2006) 051.
- [3] S. Kajita, W. Sakaguchi, N. Ohno, N. Yoshida, T. Saeki, Formation process of tungsten nanostructure by the exposure to helium plasma under fusion relevant plasma conditions, *Nucl. Fusion* 49 (2009) 095005.
- [4] K. D. Hammond, Helium, hydrogen, and fuzz in plasma-facing materials, *Materials Research Express* 4 (10) (2017) 104002. doi:10.1088/2053-1591/aa8c22. URL <https://doi.org/10.1088/2053-1591/aa8c22>
- [5] S. Takamura, Y. Uesugi, Experimental identification for physical mechanism of fiber-form nanostructure growth on metal surfaces with helium plasma irradiation, *Applied Surface Science* 356 (2015) 888 – 897. doi:<http://dx.doi.org/10.1016/j.apsusc.2015.08.112>. URL <http://www.sciencedirect.com/science/article/pii/S016943321501925X>

- of tungsten ‘fuzzy’ surfaces 415 (2011) S96–S99.
- [35] S. Pennycook, D. Jesson, High-resolution z-contrast imaging of crystals, *Ultramicroscopy* 37 (1) (1991) 14 – 38. doi:[https://doi.org/10.1016/0304-3991\(91\)90004-P](https://doi.org/10.1016/0304-3991(91)90004-P). URL <http://www.sciencedirect.com/science/article/pii/S030439919190004P>
- [36] C. M. Parish, K. Wang, R. P. Doerner, M. J. Baldwin, Grain orientations and grain boundaries in tungsten nonotendril fuzz grown under divertor-like conditions, *Scripta Materialia* 127 (2017) 132 – 135. doi:<https://doi.org/10.1016/j.scriptamat.2016.09.018>. URL <http://www.sciencedirect.com/science/article/pii/S1359646216304468>
- [37] C. M. Parish, H. Hijazi, H. M. Meyer, F. W. Meyer, Effect of tungsten crystallographic orientation on he-ion-induced surface morphology changes, *Acta Materialia* 62 (2014) 173–181. doi:<https://doi.org/10.1016/j.actamat.2013.09.045>. URL <http://www.sciencedirect.com/science/article/pii/S1359645413007301>
- [38] J.-M. Zhang, D.-D. Wang, K.-W. Xu, Calculation of the surface energy of hcp metals by using the modified embedded atom method, *Applied Surface Science* 253 (4) (2006) 2018–2024.
- [39] D.-D. Wang, J.-M. Zhang, K.-W. Xu, Anisotropy analysis of the surface energy of hcp (c/a)1.633 metals, *Surface Science* 600 (15) (2006) 2990–2996. doi:<https://doi.org/10.1016/j.susc.2006.05.012>. URL <http://www.sciencedirect.com/science/article/pii/S0039602806006078>
- [40] D. Hwangbo, S. Kajita, H. Tanaka, N. Ohno, Growth process of nano-tendril bundles with sputtered tungsten, *Nuclear Materials and Energy* 18 (2019) 250 – 257. doi:<https://doi.org/10.1016/j.nme.2019.01.008>. URL <http://www.sciencedirect.com/science/article/pii/S2352179118301145>
- [41] D. S. Sholl, R. T. Skodje, Diffusion of clusters of atoms and vacancies on surfaces and the dynamics of diffusion-driven coarsening, *Phys. Rev. Lett.* 75 (1995) 3158–3161. doi:<https://doi.org/10.1103/PhysRevLett.75.3158>. URL <https://link.aps.org/doi/10.1103/PhysRevLett.75.3158>
- [42] Developer’s web page <http://pms1.planet.sci.kobe-u.ac.jp/~seto> (accessed 2/4/2019).
- [43] M. Kumar, Y. Ando, Chemical vapor deposition of carbon nanotubes: a review on growth mechanism and mass production, *Journal of nanoscience and nanotechnology* 10 (6) (2010) 3739–3758.
- [44] E. Chason, N. Jadhav, F. Pei, E. Buchovecky, A. Bower, Growth of whiskers from sn surfaces: Driving forces and growth mechanisms, *Progress in Surface Science* 88 (2) (2013) 103 – 131. doi:<https://doi.org/10.1016/j.progsurf.2013.02.002>. URL <http://www.sciencedirect.com/science/article/pii/S007968161300004X>
- [45] V. G. Dubrovskii, G. E. Cirlin, I. P. Soshnikov, A. A. Tonkikh, N. V. Sibirev, Y. B. Samsonenko, V. M. Ustinov, Diffusion-induced growth of gaas nanowhiskers during molecular beam epitaxy: Theory and experiment, *Phys. Rev. B* 71 (2005) 205325. doi:<https://doi.org/10.1103/PhysRevB.71.205325>. URL <https://link.aps.org/doi/10.1103/PhysRevB.71.205325>
- [46] W. Boettinger, C. Johnson, L. Bendersky, K.-W. Moon, M. Williams, G. Stafford, Whisker and hillock formation on sn, sn-cu and sn-pb electrodeposits, *Acta Materialia* 53 (19) (2005) 5033 – 5050. doi:<https://doi.org/10.1016/j.actamat.2005.07.016>. URL <http://www.sciencedirect.com/science/article/pii/S1359645405004283>
- [47] Y. Sun, E. N. Hoffman, P.-S. Lam, X. Li, Evaluation of local strain evolution from metallic whisker formation, *Scripta Materialia* 65 (5) (2011) 388 – 391. doi:<https://doi.org/10.1016/j.scriptamat.2011.05.007>. URL <http://www.sciencedirect.com/science/article/pii/S1359646211002703>
- [48] V. Karpov, Electrostatic theory of metal whiskers, *Physical review applied* 1 (4) (2014) 044001.
- [49] C. Colombo, D. Spirkoska, M. Frimmer, G. Abstreiter, A. Fontcuberta i Morral, Ga-assisted catalyst-free growth mechanism of gaas nanowires by molecular beam epitaxy, *Phys. Rev. B* 77 (2008) 155326. doi:<https://doi.org/10.1103/PhysRevB.77.155326>. URL <https://link.aps.org/doi/10.1103/PhysRevB.77.155326>
- [50] B. D. Wirth, K. D. Hammond, S. I. Krashennnikov, D. Maroudas, Challenges and opportunities of modeling plasma-surface interactions in tungsten using high-performance computing, *Journal of Nuclear Materials* 463 (2015) 30 – 38, pLASMA-SURFACE INTERACTIONS 21. doi:<https://doi.org/10.1016/j.jnucmat.2014.11.072>. URL <http://www.sciencedirect.com/science/article/pii/S0022311514008757>
- [51] L. Sandoval, D. Perez, B. P. Uberuaga, A. F. Voter, Competing kinetics and he bubble morphology in w, *Phys. Rev. Lett.* 114 (2015) 105502. doi:<https://doi.org/10.1103/PhysRevLett.114.105502>. URL <https://link.aps.org/doi/10.1103/PhysRevLett.114.105502>
- [52] K. D. Hammond, B. D. Wirth, Crystal orientation effects on helium ion depth distributions and adatom formation processes in plasma-facing tungsten, *Journal of Applied Physics* 116 (14) (2014) 143301. arXiv:<https://doi.org/10.1063/1.4897419>, doi:<https://doi.org/10.1063/1.4897419>. URL <https://doi.org/10.1063/1.4897419>
- [53] R. P. Doerner, D. Nishijima, S. I. Krashennnikov, T. Schwarz-Selinger, M. Zach, Motion of w and he atoms during formation of w fuzz, *Nuclear Fusion* 58 (6) (2018) 066005. doi:<https://doi.org/10.1088/1741-4326/aab96a>. URL <https://doi.org/10.1088/1741-4326/aab96a>
- [54] K. Wang, R. Doerner, M. J. Baldwin, F. W. Meyer, M. E. Bannister, A. Darbal, R. Stroud, C. M. Parish, Morphologies of tungsten nanotendrils grown under helium exposure, *Scientific reports* 7 (2017) 42315.